A Family of Gradient Descent Grid Frequency Estimators for the SOGI Filter

José Matas, Helena Martín, Jordi de la Hoz, Abdullah Abusorrah, *Senior Member, IEEE*, Yusuf A. Al-Turki, *Senior Member, IEEE*, and Mohammed Al-Hindawi

***Abstract*—This paper applies the adaptive gradient descent method to the second-order generalized integrator (SOGI) filter in order to find an online estimation algorithm for the grid frequency, which leads to the proposal of three possible estimators. One of them is identical to the frequency-locked loop algorithm reported in the literature, which proves that it should be understood as a gradient descent estimation algorithm and not as a "frequency locked loop." The proposed gradient descent estimators are simple and suitable to be implemented into a digital processor with small computational burden. However, due to the SOGI characteristics, the estimators show to be especially sensitive to subharmonic and dc-offset voltage distortion. These problems are removed adopting a cascaded double SOGI approach, which strongly increases the rejection capability to harmonics and enhances the response to voltage sags. Simulation and experimental results are provided to validate the proposed contribution.**

***Index Terms*—Generalized integrators (GIs), gradient descent estimator, online grid-frequency estimation, power quality, second-order generalized integrator (SOGI) filter.**

NOMENCLATURE

SOGI	Second-order generalized integrator.
DSOGI	Double SOGI.
GE	Gradient estimator.
FLL	Frequency locked loop.
PLL	Phase-locked loop.
SRF-PLL	Synchronous reference frame PLL.
EPLL	Enhanced PLL.
QPLL	Quadrature PLL.
SOGI-PLL	SOGI-PLL.
IP-PLL	Inverse park-PLL.
MSOGI	Multiple-SOGI.
DPM	Dynamic phasor modeling.
LKF	Linear Kalman filter.
MAF	Moving averaging filter.
GI	Generalized integrator.
SOGI-QSG	SOGI-Quadrature signal generator.
BPF	Bandpass filter.
LPF	Low-pass filter.
HPF	High-pass filter.
NF	Notch filter.
DSP	Digital signal processor.
DAC	Digital-to-analog-converter.
ADC	Analog-to-digital converter.
SPI	Serial peripheral interface.
DSOGI-FLL-WPF	DSOGI-FLL with prefilter.
PD	Phase detector.

Manuscript received April 6, 2017; revised July 8, 2017; accepted August 26, 2017. Date of publication September 3, 2017; date of current version March 5, 2018. This work was supported by the Deanship of Scientific Research, King Abdulaziz University, Jeddah, Saudi Arabia, under Grant 24-135-35-HiCi. Recommended for publication by Associate Editor Y. Xue. *(Corresponding author: José Matas.)*

J. Matas is with the Department of Electric Engineering, Barcelona East School of Engineering, Technical University of Catalonia, Barcelona 08930, Spain, and also with the Department of Electrical and Computer Engineering, Renewable Energy Research Group, King Abdulaziz University, Jeddah 21481, Saudi Arabia (e-mail: jose.matas@upc.edu).

H. Martín and J. de la Hoz are with the Department of Electric Engineering, Barcelona East School of Engineering, Technical University of Catalonia, Barcelona 08930, Spain (e-mail: m.helena.martin@upc.edu; jordi.de.la.hoz@upc.edu).

A. Abusorrah, Y. A. Al-Turki, and M. Al-Hindawi are with the Department of Electrical and Computer Engineering, Renewable Energy Research Group, King Abdulaziz University, Jeddah 21481, Saudi Arabia (e-mail: aabusorrah@kau.edu.sa; yaturki@yahoo.com; mar7636@hotmail.com).

Color versions of one or more of the figures in this paper are available online at http://ieeexplore.ieee.org.

Digital Object Identifier 10.1109/TPEL.2017.2748920

I. INTRODUCTION

NOWADAYS, the highly distributed nature of the utility grid and the use of nonlinear loads and power electronics devices have created a growing concern for power quality problems in the grid. In this context, power inverters should perform a fast and accurate detection of grid parameters like voltage amplitude, frequency, and positive and negative sequence components of the grid voltage in order to operate during faults and network disturbances [1]–[5]. Moreover, in the case of microgrids, an accurate measurement of the frequency is required since it determines the active power balance in the transition between the islanding and grid-connected modes [6], [7].

There are several ways of obtaining the grid parameters reported in the literature for single-phase and three-phase systems, which can be grouped into frequency and time domain methods [8]–[19]. Among them, phase-locked loop (PLL) methods have become popular due to their inherent simplicity and robustness. Several PLL methods can be found in the literature for grid synchronization, such as synchronous reference frame PLL [20]–[27], enhanced PLL (EPLL) [10], [11], quadrature PLL [12], and PLL based on SOGI [23]–[26]. However, they have associated drawbacks like sensitivity to grid voltage distortions and time-response dependence on the parameters of their proportional-integral (PI) blocks.

In [27] a "frequency-locked loop" (FLL) was first introduced to tune a double SOGI (DSOGI) scheme (DSOGI-FLL) for obtaining the grid positive and negative components of the grid

frequency. The resulting FLL structure was very simple, requiring only of three math terms: a multiplication, a gain, and an integrator. The FLL was since then used to tune the SOGI filter in different applications. In [28] and [29], it was used with a "multiple SOGI" (MSOGI-FLL) structure for the fast detection of fundamental and multiple grid harmonics components under distorted grid conditions. In [30], a linearization and gain normalization using a small signal analysis of the FLL was proposed to simplify the SOGI-FLL tuning. In [31], the adaptive tuning of the frequency calculation loop gain of the SOGI-FLL and other PLL types was proposed for improving the startup and false frequency transients during phase angle perturbations. In [32], the SOGI-FLL problems with dc-offset voltage were solved by inserting a third integrator using an additional inner loop. In [33], another method of dealing with the dc-offset voltage using its estimate and removing it from the SOGI-FLL was proposed. This method leads to a simple inner algorithm without using an additional integrator, which enhances the performance of the system. In [34], the nonlinear behavior of the FLL was compensated using a fuzzy logic controller to improve the SOGI-FLL performance at the event of grid faults. In [35], a model of the SOGI-FLL was derived for the adaptive tuning of a resonant regulator for a single-phase inverter. In [36] and [37], an additional SOGI was added as a prefilter to the DSOGI-FLL in order to provide robustness against harmonics, subharmonics, and dc-offset voltage. In these last two works, a deep analysis about the SOGI tradeoff between settling time response and harmonic rejection was provided for design considerations and system tuning. In [38], a dynamic phasor modeling technique was introduced for a better analysis of stability margins of single-phase PLLs. In this paper, the SOGI-FLL was transformed to the rotating reference frame, reformulated as a PLL using a PI controller, and compared with an inverse park-PLL and EPLL. Detailed dynamics and stability boundary limits were provided for these systems arriving to the conclusion that the EPLL was adequate for networks with frequent phase-jump faults, whereas the SOGI-FLL was for networks with voltage sags. However, to this regard, it should be considered that the SOGI-FLL structure is simpler than the EPLL and that the EPLL requires of sine/cosine math functions, typically implemented with lookup tables, which increase the computation load of the system. In [39], the FLL was combined with a linear Kalman filter and used with a moving averaging filter to estimate the frequency and voltage amplitude under dc-offset voltage and harmonic distorting conditions.

Nevertheless, even though the above-described structures present high performance when estimating frequency and voltage before grid perturbations, to the authors' opinion, the application of the adaptive gradient descent method to the SOGI filter and the adoption of a DSOGI approach provides better performance when the grid is highly distorted. The proposal behaves well under different kind of distortions like subharmonics, dc-offset voltage, voltage sags, and harmonics. Regarding harmonics, the proposal shows to be very effective in environments subjected to strong distortion, especially for higher frequency components. The paper applies the adaptive gradient descent method to the SOGI filter in order to derive an online estimation algorithm for the grid frequency. The method leads to the proposal of three different estimation algorithms. The application of the adaptive gradient method has also provided the evidence that one of these algorithms is identical to the FLL structure presented in [27], which suggest that the FLL is not a "frequency locked loop" but that rather consists in a gradient descent based estimator. By doing so, this paper might have provided a better theoretical background for the FLL algorithm and to the SOGI filter, which is important for driving future research lines for the SOGI filter inside the adaptive control theory.

The derived gradient descent estimators have been proved to be simple and suitable to be implemented into a digital processor with small computational burden. However, the resulting structures were found to be sensitive to subharmonic and dc-offset voltage grid distortion. As a result, a DSOGI approach has been adopted to overcome these problems, which is analyzed and compared with the initial proposed one in order to be properly designed. The DSOGI with the gradient estimator (GE) has also been compared with the EPLL at the event of an input frequency step perturbation and their respective rejection capabilities to given harmonics have likewise been checked. The results point to DSOGI as the best suited for applications subjected to highly distorting harmonic conditions in which the rejection to the distortion is more important than the speed response, especially in the case of distortion induced by high-frequency harmonics. In these situations, the DSOGI can provide the desired filtering capability with the fastest transient allowable response due to its good tradeoff relationship between transient speed response and rejection to harmonic distortion. Moreover, the DSOGI can be useful in applications requiring extraction of the fundamental component of a signal with a high rejection to distortion, as in the case of discontinuous currents drawn by *RC*-rectifier type nonlinear loads. In this case, the DSOGI can be designed to perform a strong filtering and provide the fundamental component of the current with suitable transient response.

The paper is organized as follows. Section II performs a short description of the SOGI filter. Section III applies the gradient descent method to the SOGI structure, which leads to a family of three frequency estimators. In this section, the dynamics of the derived structures are analyzed using averaging theory and their performance in front of grid distorting conditions such as frequency step changes, harmonics, subharmonics, dc-offset voltage, and voltage sags are shown. Section IV proposes a DSOGI approach to overcome and improve the problems reported in the previous section. Section V provides experimental results to validate the proposal and Section VI performs the conclusions of this paper.

II. SOGI Filter Description

Fig. 1 depicts the structure of the SOGI filter, formed by a generalized integrator (GI) synchronized with the input v_{in} by means of an outer loop between the output v_d and v_{in}, with a gain that regulates the transient response and the bandwidth of the system [27], [36], [37]. In [27], the gain is defined as k; however, in this paper we follow the normalized version of [36] in which $k = 2\xi$, ξ being the damping factor of the system. There are some differences reported in the literature regarding

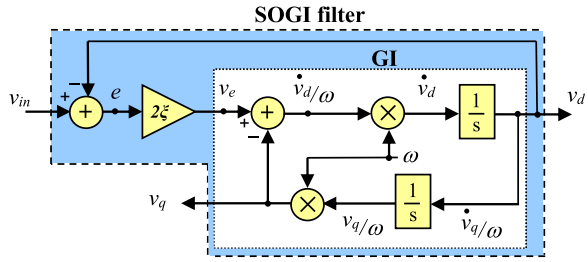

Fig. 1. Block diagram structure of the SOGI filter.

nomenclature used for the SOGI. In this paper, we use GI for the inner loop instead of SOGI or resonator, since it is responsible of the integration of sinusoidal signals. The term "SOGI filter" is used instead of SOGI quadrature signal generator along all the paper.

The SOGI outputs v_d and v_q have, respectively, bandpass filter (BPF) and low-pass filter (LPF) closed-loop transfer functions regarding v_{in}

$$H_d(s) = \frac{v_d(s)}{v_{\text{in}}(s)} = \frac{2\xi\omega \cdot s}{s^2 + 2\xi\omega \cdot s + \omega^2} \tag{1}$$

$$H_q(s) = \frac{v_q(s)}{v_{\text{in}}(s)} = \frac{2\xi\omega^2}{s^2 + 2\xi\omega \cdot s + \omega^2} \tag{2}$$

and by naming $\dot{v}_d/\omega = v_a$, the SOGI v_a and error e signals have high-pass filter (HPF) and notch filter (NF) transfer function behaviors, respectively

$$H_a(s) = \frac{v_a(s)}{v_{\text{in}}(s)} = \frac{2\xi \cdot s^2}{s^2 + 2\xi\omega \cdot s + \omega^2} \tag{3}$$

$$H_e(s) = \frac{e(s)}{v_{\text{in}}(s)} = \frac{s^2 + \omega^2}{s^2 + 2\xi\omega \cdot s + \omega^2} \tag{4}$$

where the frequency ω supplied to the GI (see Fig. 1) acts as the center frequency of the SOGI filter. Fig. 2 shows the magnitude and phase Bode plots for (1)–(4) for $\xi = 0.7$ and $\omega = 2\pi\, 50(\text{rad/s})$.

It is worth noting that when the frequency ω supplied to the GI matches the frequency ω_o of the input signal v_{in}, then the error e is canceled and the output v_d equals v_{in}.

III. Adaptive Frequency Estimation Using the Gradient Descend Method

This section applies the gradient descent method to the SOGI filter, which leads to the formulation of three possible frequency estimators and to the identification of one of them as the FLL algorithm proposed in [27]. Moreover, stability analysis and simulations to different kind of grid voltage perturbations are provided to show the behavior of the algorithms.

A. Gradient Descent Method

The gradient descent is the simplest method for optimizing an objective function or obtaining an estimate of a time-varying parameter, so suitable for being implemented in a digital processor with a small computational load [40], [41]. The gradient

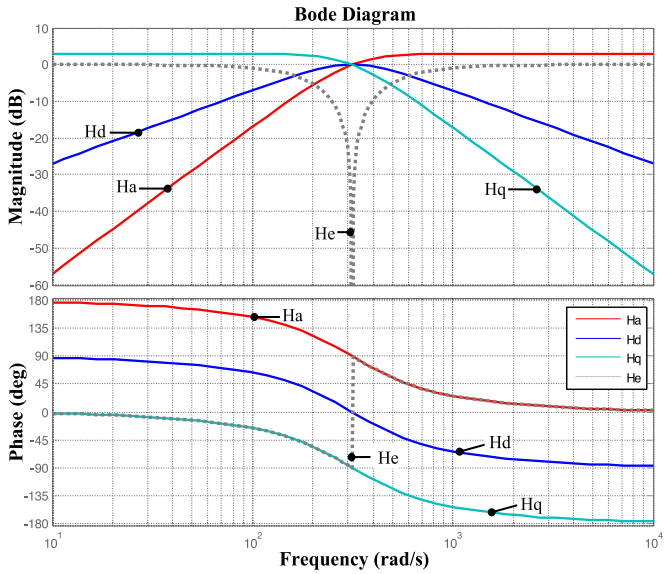

Fig. 2. Magnitude and phase Bode plots of (1)–(4) transfer functions for the SOGI filter.

descent finds a local minimum by going in the negative direction of the gradient of a function. Then, a GE algorithm for the grid frequency can be obtained for the SOGI filter by using the halved square of the error signal as an objective function

$$J(\omega) = e^2/2 \tag{5}$$

and then updating the estimate with the negative gradient of the objective function

$$\frac{d\omega}{dt} = -\gamma \cdot \frac{dJ}{d\omega} = -\gamma \cdot e \cdot \frac{de}{d\omega} \tag{6}$$

where ω is the grid frequency estimate, e is the SOGI error signal, and γ is the estimator gain.

Looking to the GI loop of Fig. 1, the relationship between e, v_a, and v_q is

$$v_a = 2\xi \cdot e - v_q. \tag{7}$$

Therefore, by doing $2\xi e = v_e$, the variable v_e may be used instead of e in (6), since this will decouple the estimator from the damping factor.

The relationship of v_q in (7) with ω can be found using its GI loop relationship with another inner variable, i.e.,

$$v_q(s) = \frac{\omega}{s} v_d(s) \tag{8}$$

from which

$$v_q = \omega \int_0^t v_d d\tau \tag{9}$$

and replacing (9) in (7) leads to

$$v_e = v_a + \omega \int_0^t v_d d\tau \tag{10}$$

and the derivative of (10) with respect to ω is

$$\frac{dv_e}{d\omega} = \int_0^t v_d d\tau = \frac{v_q}{\omega}. \tag{11}$$

Then, the expression of the frequency estimator is

$$\frac{d\omega}{dt} = -\gamma \cdot v_e \cdot \frac{v_q}{\omega}. \tag{12}$$

However, a second possible estimator can be found using v_a instead of v_q, i.e.,

$$v_d(s) = \frac{\omega}{s} v_a(s) \tag{13}$$

which, using the time expression of (13) and replacing it in (7), gives

$$v_e = \frac{\dot{v}_d}{\omega} + v_q \tag{14}$$

from which

$$\frac{dv_e}{d\omega} = -\frac{\dot{v}_d}{\omega^2} = -\frac{v_a}{\omega}. \tag{15}$$

Therefore, a second frequency estimator is formulated as

$$\frac{d\omega}{dt} = \gamma \cdot v_e \cdot \frac{v_a}{\omega}. \tag{16}$$

Finally, the relationship of v_a and v_q can be also used to find a third estimator, i.e.,

$$v_e = \frac{\dot{v}_d}{\omega} + \omega \int_0^t v_d d\tau \tag{17}$$

from which

$$\frac{dv_e}{d\omega} = \frac{1}{\omega}(v_q - v_a). \tag{18}$$

And a third estimator is

$$\frac{d\omega}{dt} = \frac{\gamma}{2} \cdot \frac{v_e}{\omega} \cdot (v_a - v_q). \tag{19}$$

Notice that the third estimator is simply a combination of previous two in (12) and (16), and that the gain is negative when using v_q and positive when using v_a. Then, the third estimator has a double gain value regarding the others because it has two active signal paths, so its gain should be divided by two.

B. System Stability

The SOGI filter with one of the previously derived estimators constitutes together a highly nonlinear and coupled system, which is not easy to analyze for oscillatory forcing inputs. This system evolves in two time scales, a fast oscillatory one linked to the independent variable *t* for the states and a slow one for the estimated frequency ω, provided the gain γ in its update equation is small. Then, the integral manifold approach to slow adaptation concept along with the averaging theory [42], [43] can be here applied to show that for a periodic input signal

$$v_{\text{in}} = A_{\text{in}} \sin(\omega_o t + \varphi) \tag{20}$$

the system will be locally asymptotically stable at the equilibrium point

$$\left(v_d, \frac{v_q}{\omega}, \omega\right) = \left(A_{\text{in}} \sin(\omega_o t + \varphi), -\frac{A_{\text{in}}}{\omega_o} \cos(\omega_o t + \varphi),\ \omega_o\right) \tag{21}$$

for a small enough gain γ. Thus, considering that the GI transfer function, from v_q to v_e, is

$$\frac{v_q(s)}{v_e(s)} = \frac{\omega^2}{s^2 + \omega^2} \tag{22}$$

and introducing the time version of (22) in (12), it gives

$$\frac{d\omega}{dt} = -\frac{\gamma}{\omega^3}(\ddot{v}_q + \omega^2 v_q) v_q. \tag{23}$$

As the dynamics of ω is assumed much slower than the dynamics of the states, the transients in the GI can be ignored, allowing for separation of the GE update equation (23) from the state equation of the SOGI filter. Then, the update law can be approximated as

$$\begin{aligned} \frac{d\omega}{dt} &= -\frac{\gamma}{\omega^3}\left(\omega^2 - \omega_o^2\right) v_q^2 \\ &= -\frac{\gamma}{\omega^3}(\omega^2 - \omega_o^2) A_{\text{in}}^2 G_q^2(j\omega_o, \omega) \cos^2(\omega_o t + \varphi) \end{aligned} \tag{24}$$

since, at steady state, for a sinusoidal input (20), it holds $\ddot{v}_q = -\omega_o^2 v_q$ and $v_q = -AG_q(j\omega_o, \omega)\cos(\omega_o t + \varphi)$ $v_q = -A_{\text{in}} G_q(j\omega_o, \omega)\cos(\omega_o t + \varphi)$, where $G_q(j\omega_o, \omega)$ is the gain of (2).

The fast oscillatory dynamics in (24) can now be averaged through time integration

$$\frac{d\omega_{\text{av}}}{dt} = \frac{1}{T}\int_t^{t+T} f\left(\omega_{\text{av}}, \tau\right) d\tau = f_{\text{av}}\left(\omega_{\text{av}}\right) \tag{25}$$

where the subscript $_{\text{av}}$ represents an averaged value. Thus, calculating the averaged value of (24), it is obtained

$$\frac{d\omega_{\text{av}}}{dt} = -\gamma \frac{2\xi^2 A_{\text{in}}^2 \omega_{\text{av}} (\omega_{\text{av}}^2 - \omega_o^2)}{\left(\omega_{\text{av}}^2 - \omega_o^2\right)^2 + \left(2\xi \omega_{av} \omega_o\right)^2} \tag{26}$$

which retains only the mean behavior of (24) and is a time-invariant system to which standard techniques for stability analysis can be applied. It can be observed that the averaged dynamics in (26) has an isolated equilibrium point at $\omega_{\text{av}} = \omega_o$. So, computing the first-order linearization of (26) around this isolated equilibrium point, we obtain the dynamics

$$\dot{\bar{\omega}}_{\text{av}} = -\frac{\gamma A_{\text{in}}^2}{\omega_0^2} \cdot (\bar{\omega}_{\text{av}} - \omega_o) \tag{27}$$

which is asymptotically stable. This result implies in turn the local asymptotical stability of the GE update law in (12) around $\omega = \omega_o$.

When the same procedure is applied to the second estimator in (16) (see the Appendix), the same first-order linearized expression (27) is obtained, as is also the case for the third estimator in (19), since it is a combination of (12) and (16). So, it can be concluded that these estimators are likewise locally asymptotically stable around $\omega = \omega_o$.

Moreover, (27) can be normalized choosing a gain

$$\gamma = \frac{\omega^2}{A_{\text{in}}^2} \lambda \tag{28}$$

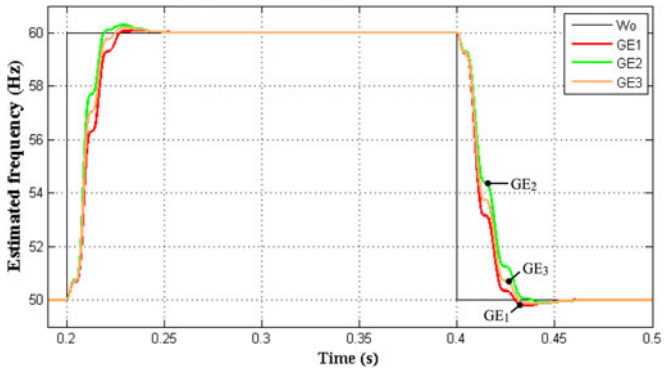

Fig. 3. Transient response of the SOGI-GEs for a grid voltage frequency step perturbation from 50 to 60 Hz and then back to 50 Hz.

which implies sensing ω from the own GE output and dividing it by A_{in}^2. The square of A_{in} is estimated using v_d and v_q as in

$$A^2 = v_d^2 + v_q^2 \tag{29}$$

where A is the estimate of A_{in}, resulting in the following first-order transfer function

$$\frac{\bar{\omega}_{\text{av}}(s)}{\omega_o(s)} = \frac{\lambda}{s+\lambda}. \tag{30}$$

Considering the normalization in (28), the GEs (12), (16), and (19) turn to be

$$\frac{d\omega_1}{dt} = -\lambda_1 \cdot \frac{\omega_1}{A_{\text{in}}^2} v_e v_q \tag{31}$$

$$\frac{d\omega_2}{dt} = \lambda_2 \cdot \frac{\omega_2}{A_{\text{in}}^2} v_e v_a \tag{32}$$

$$\frac{d\omega_3}{dt} = \lambda_3 \cdot \frac{\omega_3}{A_{\text{in}}^2} v_e (v_a - v_q) \tag{33}$$

where the frequency subscripts distinguish the particular GEs. Note that with the normalization of (28), the divisions by ω in the expressions (12), (16), and (19) have been removed, simplifying the algorithms implementation.

At this point, it can be seen that the structure of GE_1 in (31) with a SOGI filter (SOGI-GE_1) is identical to the normalized SOGI-FLL proposed in [27]. This suggest that the FLL is a gradient descent estimator and not a "frequency locked loop" and that its theoretical background lies better inside the adaptive control theory, which points out the direction that the future research should follow for improving this structure.

C. Frequency Step Transient Response

Fig. 3 shows the simulation results for the SOGI-GE_1, GE_2, and GE_3 in (31)–(33) using MATLAB/Simulink software. The simulations were carried out simultaneously, each GE with its own SOGI filter, in order to compare the results. The damping factors and estimator gains were set to $\xi_1 = \xi_2 = \xi_3 = 0.7$ and $\lambda_1 = \lambda_2 = \lambda_3 = 88(\text{s}^{-1})$, respectively. The GE integrators were initialized to $\omega_o = 2\pi 50(\text{rad/s})$. These values were chosen to obtain an underdamped transient response with a 1% overshoot for the SOGI-GE_1 to a step frequency perturbation from 50 to 60 Hz and then back to 50 Hz.

In Fig. 3, it can be seen that the transients can be assimilated to quasi-second-order responses that have small differences during the step-up and step-down events. In particular, it can be seen that GE_2 is faster at the step up, but slower at step down. On the contrary, GE_1 is slower at the step up, but faster at step down. The response is more equilibrated for GE_3, which is in the middle. This particular behavior can be explained by the asymmetrical Bode magnitude plots of v_a and v_q, which, respectively, have HPF and LPF transfer functions (see Fig. 2). Therefore, at the step up v_a provides an output signal with gain $20\log(2\xi)$ (3 dB in this case), whereas v_q is attenuated -40 dB/decade. However, at the step down v_a is attenuated -40 dB/dec, whereas v_q is affected by the $20\log(2\xi)$ (3 dB) gain. Notice that for GE_3, the gain asymmetry is compensated by the mix of v_a and v_q, and its response at both transients shows to be more equilibrated, between GE_1 and GE_2. The gain asymmetry is also responsible of achieving small differences in the experienced overshoot values. The obtained overshoots were of 1%, 3%, and 2% for GE_1, GE_2, and GE_3, respectively.

D. Harmonic, Subharmonic, and DC-Offset Voltage Rejection

At the event of grid voltage distortion such as harmonics, subharmonics and dc-offset voltage, the performance of the SOGI filter and the GEs is affected. These distortions first impact the SOGI filter outputs and then the estimated frequency through the multiplication of the SOGI outputs v_a or v_q by the SOGI error v_e.

The SOGI filter outputs have different transfer functions [see (1)–(3)] so there will be different effects depending on the distortion type. On the one hand, v_a and v_q have, respectively, HPF and LPF transfer functions, so harmonics are going to be transferred directly to v_a with $20\log(2\xi)$ gain, and dc-offset voltage and subharmonics are going to be conveyed to v_q with also $20\log(2\xi)$ gain (see Fig. 2). Moreover, the estimated grid voltage amplitude obtained through the square root of A^2 is also distorted with subharmonics and dc-offset voltage via v_q.

On the other hand, the distortion is conveyed to the v_e signal through its NF transfer function behavior [see (4)], so the multiplication of v_e by v_a or v_q generates new frequencies components: ones pulsating at the sum of the v_e and v_a or v_q frequencies and others pulsating at the subtraction between v_e and v_a or v_q frequencies. As a particular case, when the frequency of the distortions in v_e and v_a or v_q is the same, their subtraction will give rise to zero frequency, or dc components, which will induce deviations in the mean value of the estimated grid frequency, further worsening the overall problem.

Additionally, the outputs of the GEs laws (31)–(33) must be integrated in order to supply the estimated frequency to the SOGI filter. The required integrators will act as a LPF filters with attenuation -20 dB/dec for frequencies above 1 rad/s. Thus, the distorting components closer to this cutoff frequency will be less attenuated than higher order harmonics.

In order to illustrate the impact of these distortions, Fig. 4 depicts the GE_1, GE_2, and GE_3 responses to several

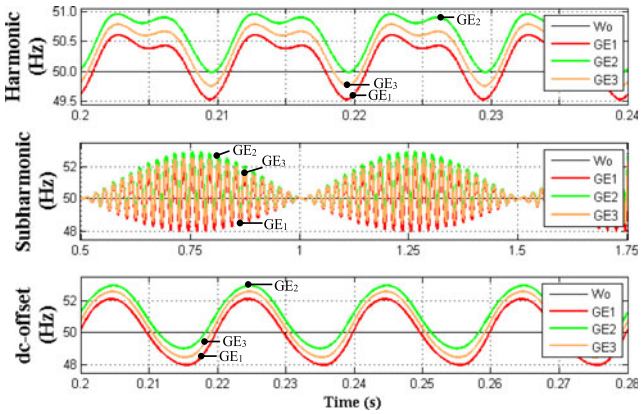

Fig. 4. Estimated frequency time responses of the SOGI-GEs to distorted grid voltage components of 10% amplitude. Upper: 3rd harmonic. Middle: 1-Hz subharmonic. Bottom: dc-offset voltage.

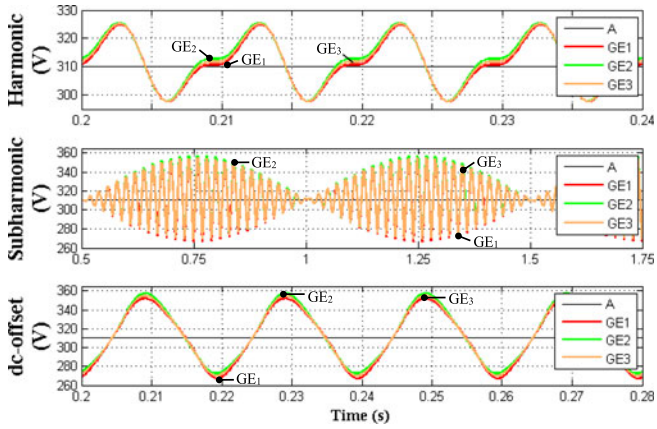

Fig. 5. Estimated voltage amplitude time responses using (29) in the SOGI-GEs to distorted grid voltage components of 10% amplitude. Upper: 3rd harmonic. Middle: 1-Hz subharmonic. Bottom: dc-offset voltage.

TABLE I
ESTIMATED FREQUENCY PEAK-TO-PEAK AMPLITUDE DISTORTION AND MEAN DEVIATION FROM ω_o FOR THE CASES DEPICTED IN FIG. 4

Peak-to-peak amplitude (Hz)	GE_1	GE_2	GE_3
3rd harmonic	1.08	0.96	1.03
1-Hz subharmonic and dc offset	4.12	3.93	4.10
Mean deviation from ω_o at steady state (Hz)			
3rd harmonic	0.07	0.47	0.27
1-Hz subharmonic and dc offset	0.04	0.98	0.51

TABLE II
PEAK-TO-PEAK AMPLITUDE OF THE DISTORTION IN THE ESTIMATED GRID VOLTAGE AMPLITUDE AND MEAN DEVIATION FROM THE NOMINAL *A* LEVEL FOR THE CASES DEPICTED IN FIG. 5

Peak-to-peak amplitude (V)	GE_1	GE_2	GE_3
3rd harmonic	27.30	27.60	27.50
1-Hz subharmonic and dc offset	76.00	84.80	84.90
Mean deviation from *A* at steady state (V)			
3rd harmonic	1.05	1.40	1.25
1-Hz subharmonic and dc offset	3.9	4.95	2.15

distorting components with 10% of nominal amplitude, namely a third harmonic, a 1-Hz subharmonic, and dc-offset voltage. The peak-to-peak amplitude and the mean deviation from ω_o of the estimated frequency have been measured and listed in Table I. As the measurements for the subharmonic and dc-offset cases are identical, they have been put together in a single row of Table I.

In Fig. 4 and Table I, it can be seen that the peak-to-peak amplitude of the frequency distortion is around 1 Hz for the third harmonic case (upper plot) and 4 Hz for the subharmonic and dc-offset cases (middle and bottom cases, respectively). As mentioned before, the greater distorting capacity of subharmonics and dc-offset voltage is due to its low frequency components, which are less filtered by the integrator present in the GEs structures. Moreover, it can be seen that the mean value of the frequency deviates upward from the nominal 50-Hz level due to the distortion. The GE_1 is the estimator presenting less deviation, whereas GE_2 is the most affected.

In the same way, Fig. 5 depicts the estimated grid voltage amplitudes of the SOGI-GEs to the same distorting components considered in Fig. 4. The peak-to-peak amplitude of the distortion induced in the estimated values of the grid voltage amplitude and the deviation of their mean values from the nominal voltage level *A* has been listed in Table II.

E. Response to Voltage Sags

The impact of voltage sags on the estimated frequency increases with the sag depth. Consequently, the performance of the SOGI-GEs will be tested under a sag of 80% depth, i.e., the maximum depth for which some grid codes require ride-through capability of wind turbines. To this regard, Fig. 6 shows the transient responses to a voltage sag with 80% depth in the input voltage at 0.2 s. It can be seen in the left subplot that the frequency perturbations reach peak-to-peak amplitudes of 12.85 Hz for GE_1, 17.83 Hz for GE_2, and 13.23 Hz for GE_3. Then, due to the HPF behavior of the v_a signal present in GE_2, this structure is more sensible to the high-frequency components

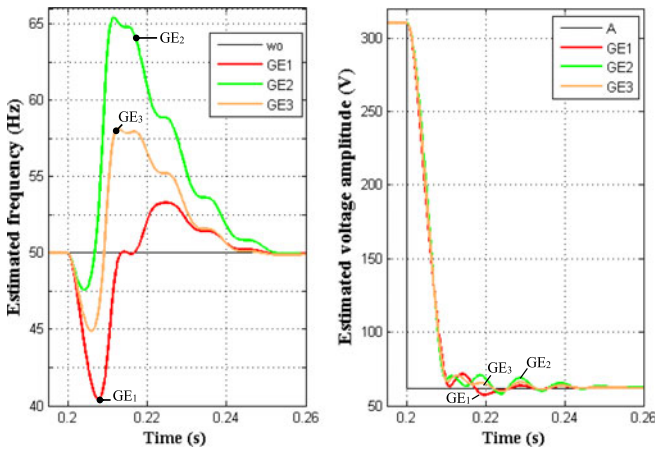

Fig. 6. SOGI-GEs estimated grid frequency and voltage amplitude for an 80% voltage sag.

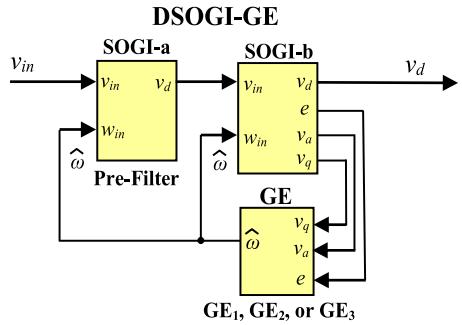

Fig. 7. DSOGI-GE with prefilter structure.

introduced in the perturbation, while GE_1 and GE_3 have similar responses. The transients last 43 ms for GE_1 and GE_3 and 51 ms for GE_2. In the right subplot of Fig. 6, it can be seen that the transient responses for the estimated voltage amplitudes are all similar, with small oscillations that last about 42 ms.

As summary of this section, harmonics, subharmonics, and dc-offset voltage components cause distorted oscillations and deviations of the mean values in the estimated frequency and voltage amplitude from their actual levels. Specially, subharmonic and dc-offset voltage have a higher distortion capacity. Additionally, voltage sags have a high distorting capacity. It is important to remark that all these problems are common to all the SOGI-related structures, like the SOGI-FLL, DSOGI-FLL, and MSOGI-FLL [27]–[36].

IV. DSOGI Approach

Part of the described problems can be solved adopting a DSOGI approach as represented in Fig. 7, that uses an additional SOGI as a "bandpass prefilter" to remove the distortion caused by subharmonics and dc-offset voltage, increasing the rejection capacity of the system.

For ease of design, this DSOGI system is designed with equal damping factors, $\xi_a = \xi_b = \xi$. Then, the transfer function of the DSOGI outputs regarding v_{in} corresponds to those of (1)–(4) with an additional cascaded BPF transfer function. From a filter point of view, v_d, v_a, and v_q from SOGI-b block have -40dB/dec, -60dB/dec, and -20dB/dec magnitude attenuations to subharmonics, respectively, and -40dB/dec, -20dB/dec, -60dB/dec magnitude attenuations to harmonics, respectively. So, the DSOGI has a better rejection capability than the SOGI approach.

A. Frequency Step Transient Response

The transient response of the DSOGI-GEs for a frequency step perturbation is slower than the obtained for the SOGI one due to the higher order of the structure. The DSOGI is a fourth-order system and the SOGI a second-order one. On the other hand, the GEs gains for this DSOGI approach had to be reduced from 88 to $49.3(\mathrm{s}^{-1})$ in order to obtain the same 1% overshoot for the GE_1 than in the previous case. As a result of the order increase and the gain reduction, the DSOGI-GEs transient response shows an extra 21-ms delay. Fig. 8 depicts the transient response for a sudden frequency step change from

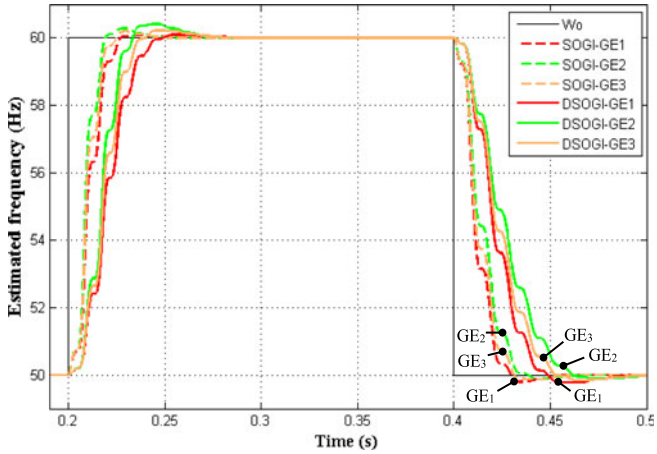

Fig. 8. DSOGI-GEs transient responses to a grid voltage frequency step perturbation from 50 to 60 Hz and then back to 50 Hz. DSOGI-GEs: (solid lines). SOGI-GEs: (dashed lines).

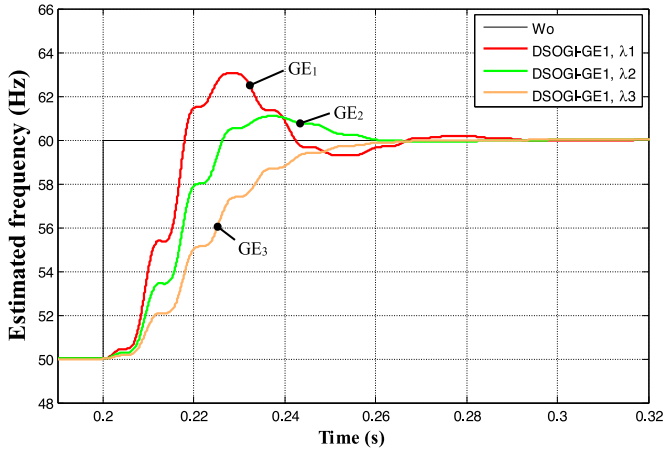

Fig. 9. DSOGI-GE_1 transient responses to a grid voltage frequency step perturbation from 50 to 60 Hz for three different GE_1 gains $\lambda_1 = 119.3$, $\lambda_2 = 72.2$, and $\lambda_3 = 42.4$.

50 to 60 Hz and then back to 50 Hz. The SOGI-GEs responses are also plotted in Fig. 8 using dashed lines for comparison purposes. As in the SOGI case, for DSOGI-GE_2 and GE_3 the obtained overshoots are different from the expected 1% due to their asymmetric gain characteristics, namely 4.2% and 2.3%, respectively.

Alternatively, the Fig. 9 depicts the transient response of only the DSOGI-GE_1 for three different estimator gains, i.e., $\lambda_1 = 119.3$, $\lambda_2 = 72.25$, and $\lambda_3 = 42.4$, in order to see how the response relies in the pair of gains (ξ, λ). These gains have been tuned for obtaining overshoots M_p of 30%, 15%, and 0%, respectively.

B. Harmonic, Subharmonic, and DC-Offset Voltage Rejection

The rejection capability to subharmonics and dc-offset highly increases with the DSOGI approach, to a point in which the perturbation to the 1-Hz subharmonic is strongly reduced and the dc-offset voltage is removed. The rejection capability to

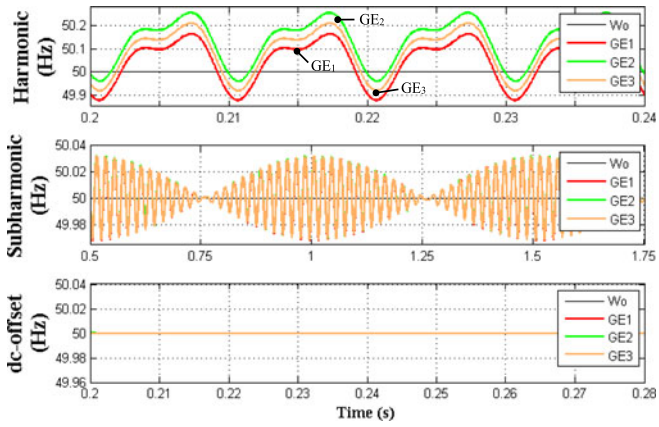

Fig. 10. Estimated frequency time responses of the DSOGI-GEs to distorted grid voltage components of 10% amplitude. Upper: 3rd harmonic. Middle: 1-Hz subharmonic. Bottom: dc-offset voltage.

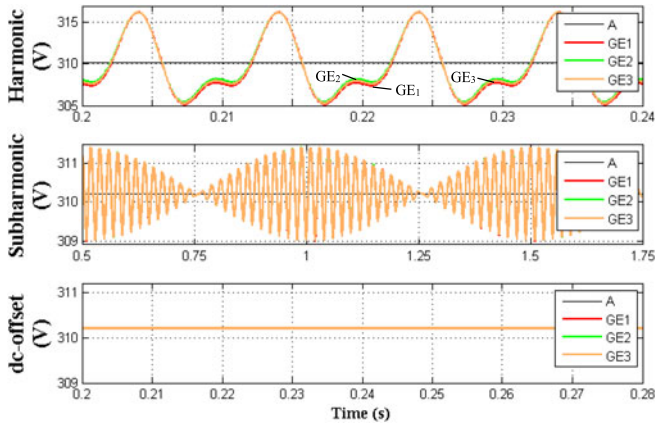

Fig. 11. Estimated voltage amplitude time responses using (29) in the DSOGI-GEs to distorted grid voltage components of 10% amplitude. Upper: 3rd harmonic. Middle: 1-Hz subharmonic. Bottom: dc-offset voltage.

TABLE III
ESTIMATED FREQUENCY PEAK-TO-PEAK AMPLITUDE DISTORTION AND MEAN DEVIATION FROM ω_o FOR THE CASES DEPICTED IN FIG. 10

Peak-to-peak amplitude (Hz)	GE_1	GE_2	GE_3
3rd harmonic	0.29	0.30	0.29
1-Hz subharmonic	0.06	0.06	0.06
DC offset	0.00	0.00	0.00
Mean deviation from ω_o at steady state (Hz)			
3rd harmonic	0.02	0.11	0.06
1-Hz subharmonic and dc offset	0.00	0.00	0.00

harmonics also increases considerably. As for the single SOGI case, Figs. 10 and 11 depict the DSOGI-GEs responses to the same distorting components with 10% of nominal amplitude: a third harmonic, a 1-Hz subharmonic, and dc-offset voltage.

The peak-to-peak amplitude and the mean deviation from ω_o of the estimated frequency and from nominal A of the estimated grid voltage amplitude are listed in Tables III and IV, respectively. These data have been compared with those in Tables I and II to assess the achieved percentage reductions, which are shown in Table V.

TABLE IV
PEAK-TO-PEAK AMPLITUDE OF THE DISTORTION IN THE ESTIMATED GRID VOLTAGE AMPLITUDE AND MEAN DEVIATION FROM THE NOMINAL A LEVEL FOR THE CASES DEPICTED IN FIG. 11

Peak-to-peak amplitude (V)	GE_1	GE_2	GE_3
3rd harmonic	11.04	10.85	10.95
1-Hz subharmonic	2.40	2.40	2.40
DC offset	0.00	0.00	0.00
Mean deviation from A at steady state (V)			
3rd harmonic	0.47	0.57	0.52
1-Hz subharmonic and dc offset	0.00	0.00	0.00

TABLE V
DISTORTION PERCENTAGE REDUCTION ACHIEVED BY THE DSOGI-GEs

3rd harmonic percentage reduction (%)	GE_1	GE_2	GE_3
Estimated frequency	**73.15**	**68.75**	**71.84**
Estimated amplitude voltage	**59.55**	**60.70**	**60.20**
1-Hz subharmonic percentage reduction (%)			
Estimated frequency	**98.47**	**98.40**	**98.46**
Estimated amplitude voltage	**96.84**	**97.17**	**97.17**
3rd harmonic mean deviation percentage reduction (%)			
Estimated frequency	**85.71**	**76.60**	**77.78**
Estimated amplitude voltage	**55.05**	**59.07**	**58.20**

TABLE VI
SOGI-GE_1 AND DSOGI-GE_1 PEAK-TO-PEAK AMPLITUDE DISTORTION OF THE ESTIMATED FREQUENCY AND VOLTAGE AMPLITUDE FOR HARMONIC ORDERS 3RD, 5TH, 7TH, AND 11TH WITH 10% AMPLITUDE

Peak-to-peak frequency distortion (Hz) at harmonic order h	3rd	5th	7th	11th
SOGI-GE_1	1.08	0.54	0.34	0.25
DSOGI-GE_1	0.29	0.06	0.03	0.01
Percentage reduction (%)	**73.14**	**88.88**	**91.17**	**96.00**
Peak-to-peak amplitude distortion (V) at harmonic order h				
SOGI-GE_1	27.30	11.94	8.71	5.59
DSOGI-GE_1	11.04	2.37	1.23	0.50
Percentage reduction (%)	**59.56**	**80.09**	**85.82**	**90.93**

The showed responses and data clarify that the DSOGI-GEs have a strong rejection to subharmonics and to dc-offset voltage. However, in the case of harmonics it is important to understand that the DSOGI-GEs rejection relies on three factors: to the harmonic attenuation at the DSOGI outputs, to the harmonic attenuation at the error signal, and to the GEs gain. The harmonic attenuation increases with the harmonic frequency, due to the fourth-order BPF characteristic of the DSOGI. Then, in order to evaluate all these factors together and see how they affect every harmonic distortion depending on its frequency, Table VI shows the peak-to-peak amplitudes of the distortions in the estimated frequency and the estimated voltage amplitude of GE_1, for harmonic components of order $h = 3$, 5, 7, 11 with 10% amplitude. Looking at this table, it can be seen that the harmonic rejection increases progressively with the harmonic

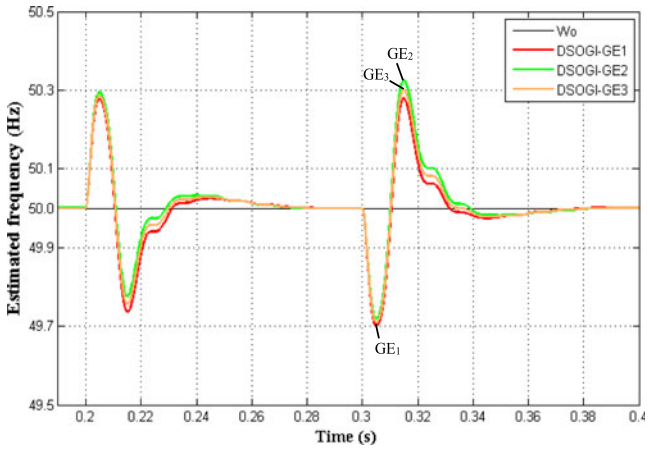

Fig. 12. DSOGI-GEs transient response to a dc-offset voltage perturbation from 0% to 10% of nominal amplitude at 0.2 s and then back to 0% at 0.3 s.

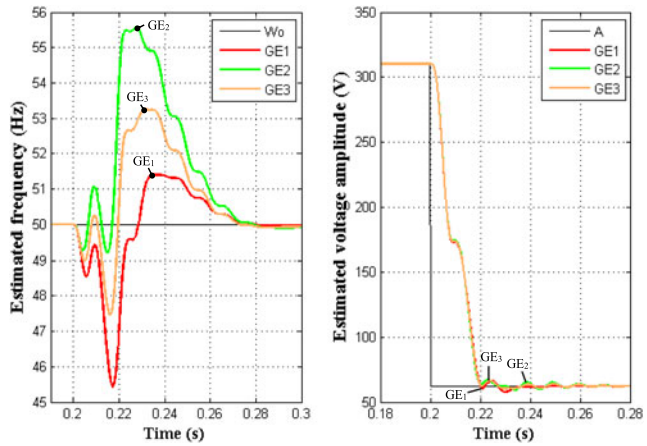

Fig. 13. DSOGI-GEs estimated grid frequency and voltage amplitude for an 80% voltage sag.

order h. Hence, the harmonics are attenuated strongly for $h > 5$, the lower harmonics being those who have higher distorting capacity on the estimated parameters.

C. DC-Offset Voltage Transient Response

Although the DSOGI-GEs reject the dc-offset voltage at steady state (see Fig. 10, bottom subplot), it is interesting to see how the time response to a dc-offset voltage transient is. Fig. 12 depicts the response to a sudden 10% amplitude dc-offset voltage perturbation at 0.2 s and then back to normal conditions at 0.3 s. In this figure, it can be seen that the perturbation impact on the DSOGI-GEs estimations is small, being its peak magnitude near 0.3 Hz for all the cases. Note that the transient disappears after 80-ms duration. Then, it can be concluded that the response of the DSOGI-GEs is notably improved regarding the SOGI-GEs (see Fig. 4, bottom subplot).

D. Response to Voltage Sags

Fig. 13 depicts the transient response to an 80% depth voltage sag in the input voltage at 0.2 s. Table VII summarizes the

TABLE VII
CHARACTERISTICS OF SOGI-GEs AND DSOGI-GEs FREQUENCY PERTURBATIONS FOR AN 80% DEPTH VOLTAGE SAG AND ACHIEVED DISTORTION REDUCTIONS

	GE_1	GE_2	GE_3
SOGI-GEs upper peak from 50 Hz (Hz)	3.29	15.40	8.11
DSOGI-GEs upper peak from 50 Hz (Hz)	1.40	5.56	3.24
SOGI-GEs lower peak from 50 Hz (Hz)	9.57	2.43	5.12
DSOGI-GEs lower peak from 50 Hz (Hz)	4.55	0.79	2.54
SOGI-GEs peak-to-peak amplitude (Hz)	12.85	17.83	13.23
DSOGI-GEs peak-to-peak amplitude (Hz)	5.95	6.35	5.78
Percentage amplitude reduction (%)	**53.69**	**64.38**	**56.31**
SOGI-GEs transient duration (ms)	52.50	52.50	52.50
DSOGI-GEs transient duration (ms)	80.00	80.00	80.00
Percentage transient duration increase (%)	**52.38**	**52.38**	**52.38**

TABLE VIII
PEAK-TO-PEAK AMPLITUDE OF THE FREQUENCY PERTURBATION PRODUCED BY VOLTAGE SAGS WITH DIFFERENT DEPTH LEVELS

Voltage sag depth level	GE_1	GE_2	GE_3
60%—SOGI-GEs	5.49	5.03	4.63
60%—DSOGI-GEs	2.17	1.79	1.92
Percentage reduction (%)	**60.47**	**64.41**	**58.53**
40%—SOGI-GEs	2.89	2.61	2.69
40%—DSOGI-GEs	1.16	0.99	1.06
Percentage reduction (%)	**59.80**	**62.07**	**60.59**
20%—SOGI-GEs	1.27	1.19	1.14
20%—DSOGI-GEs	0.49	0.45	0.47
Percentage reduction (%)	**61.42**	**62.18**	**58.77**

obtained data and compares them with those of previous section for the SOGI-GEs. It can be concluded that the DSOGI-GEs improve the response to voltage sags, entailing a significant perturbation amplitude reduction with respect to the SOGI-GEs approach, though with an increased transient duration. Fig. 13 also shows that regarding the peak-to-peak perturbations in the estimated voltage amplitude, the differences between the GEs are small and that the oscillations have a smaller amplitude that those achieved by the SOGI-GEs. Additionally, Table VIII shows the peak-to-peak amplitude distortion produced for 60%, 40%, and 20% depth voltage sags. This table illustrates the magnitude of the distortion induced by the voltage sags for different depth levels. As can be seen, the DSOGI-GEs improve the response to voltage sags for all the cases, with a percentage reduction around 60%.

As a conclusion to this section, it can be said that the DSOGI approach supposes a great improvement in the distortion rejection capability of the system, but at the expense of an increased duration of the transient response to step frequency perturbations. However, as the transient duration increase is around a single time period of the grid voltage, it can be considered that the overall performance is improved in view of the high rejection capability achieved.

E. Comparison With the EPLL in Terms of Transient Response Time and Rejection to Harmonics

This part compares the DSOGI-GE_1 with the EPLL considering only the tradeoff between dynamic response speed and

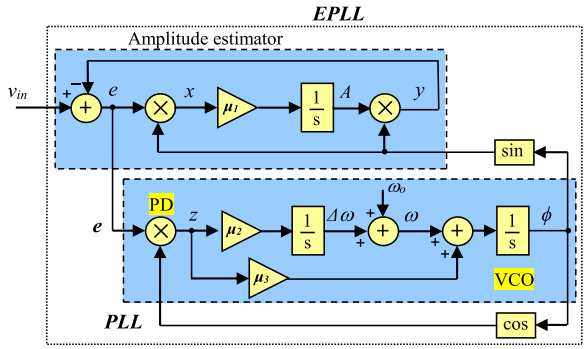

Fig. 14. Block diagram of the EPLL.

rejection to harmonics. Although these two structures are different in conception, since one is a PLL and the other is a frequency estimator, the EPLL has been selected as a benchmark as it could be thought of as the simplest and most widely known structure suitable for synchronization in power applications. The aim is to highlight the response time versus harmonic rejection tradeoff and its dependence on the EPLL and the DSOGI-GE$_1$ gains, identifying which could be the appropriate applications for the DSOGI-GE$_1$.

By adding an input signal amplitude estimator to the PLL (see Fig. 14), the EPLL achieves removal of the double frequency component present in the conventional PLL for pure input sinusoidal signals [32], [44].

Following the reasoning in [44], the EPLL linearized small signal frequency transfer function can be put as

$$\frac{\omega(s)}{\omega_o(s)} = \frac{\omega_r^2}{s^2 + 2\xi_r\omega_r \cdot s + \omega_r^2} \tag{34}$$

where ω_o is the frequency of v_{in} and ω its estimate, ξ_r is the damping factor and ω_r is the center frequency. In turn, the dependence of the EPLL gains on ξ_r and ω_r is $\mu_2 = \omega_r^2 2/A_{\text{in}}$ and $\mu_3 = 4\xi_r \cdot \omega_r/A_{\text{in}}$, where A_{in} is the amplitude of v_{in}. The model in (34) can be used for setting the overshoot M_p and peak time t_p of the EPLL transient frequency response.

Consequently, the gains of the EPLL were tuned to simulate two different frequency transient responses to a grid frequency change from 50 to 60 Hz. Both responses present $M_p = 1\%$, but the faster has $t_{p1} = 0.046\,\text{s}$, $(\xi_r,\, \omega_r) = (0.83,\, 125)$, and the slower has $t_{p2} = 0.1\,\text{s}$, $(\xi_r,\, \omega_r) = (0.83,\, 55)$, respectively. Then, the DSOGI-GE$_1$ parameters were tuned to produce two frequency transient responses to the same grid frequency change with the same performance indexes, namely $M_p = 1\%$ and $t_{p1} = 0.046\,\text{s}$, $(\xi,\, \lambda) = (0.975,\, 67.23)$, and $M_p = 1\%$ and $t_{p2} = 0.1\,\text{s}$, $(\xi,\, \lambda) = (0.405,\, 29.56)$. The obtained EPLL and DSOGI-GE$_1$ frequency transient responses have been jointly represented in the upper subplot of Fig. 15.

Then, with the EPLL and the DSOGI-GE$_1$ tuned as explained above, the peak-to-peak amplitudes of the distortion in their estimated frequencies were evaluated for harmonic components in v_{in} of order $h = 3,\, 5,\, 7,\, 11$ with 10% of amplitude. The results have been displayed in the lower subplot of Fig. 15 and also have been collected at Table IX.

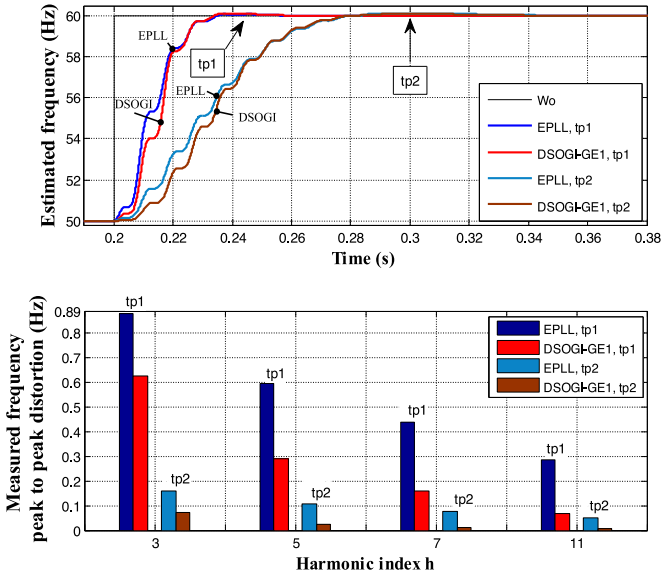

Fig. 15. Up: EPLL and DSOGI-GE$_1$ frequency transient responses to a grid frequency step perturbation from 50 to 60 Hz, with $M_p = 1\%$ and $t_{p1} = 0.046\,\text{s}$ and with $M_p = 1\%$ and $t_{p2} = 0.1\,\text{s}$. Down: Peak-to-peak amplitude distortions of the estimated frequency for harmonic orders 3rd, 5th, 7th, and 11th with 10% amplitude.

TABLE IX
EPLL AND DSOGI-GE$_1$ PEAK-TO-PEAK AMPLITUDE DISTORTION OF THE ESTIMATED FREQUENCY FOR HARMONIC ORDERS 3RD, 5TH, 7TH, AND 11TH WITH 10% AMPLITUDE

Peak-to-peak frequency distortion (Hz) at harmonic order h	3rd	5th	7th	11th
EPLL, t_{p1}	0.878	0.596	0.440	0.286
DSOGI-GE$_1$, t_{p1}	0.626	0.292	0.157	0.065
Percentage reduction (%)	**28.70**	**51.01**	**64.32**	**77.27**
EPLL, t_{p2}	0.161	0.105	0.078	0.051
DSOGI-GE$_1$, t_{p2}	0.071	0.025	0.012	0.005
Percentage reduction (%)	**55.90**	**76.19**	**84.62**	**90.20**

As can be seen in Fig. 15 and Table IX, the harmonic impact in the estimated frequency is strongly related with t_p, i.e., faster transient responses are more affected by harmonics. Nevertheless, this impact is greater in the EPLL than in the DSOGI-GE$_1$. The higher order of the DSOGI-GE$_1$ endows it with a stronger harmonic rejection capability than the EPLL. Then, the DSOGI-GE$_1$ can be more suitable for applications affected by highly distorted conditions in which the speed response is not a crucial requirement, and it behaves particularly well specially for higher harmonics. Consequently, the DSOGI-GEs superior rejection capabilities make these structures less sensible to small perturbations induced by noise of different nature and other errors produced in the digital implementation.

In another test scenario, the DSOGI-GE$_1$ was tuned with the pair $(\xi,\, \lambda) = (0.68, 48.38)$ to achieve the same peak-to-peak amplitude distortion in the estimated frequency than the EPLL for the fifth harmonic and $t_{p2} = 0.1\,\text{s}$ case of Table IX (see upper subplot of Fig. 16).

As can be seen in the lower subplot of Fig. 16, matching the harmonic impact in both structures turns faster the transient

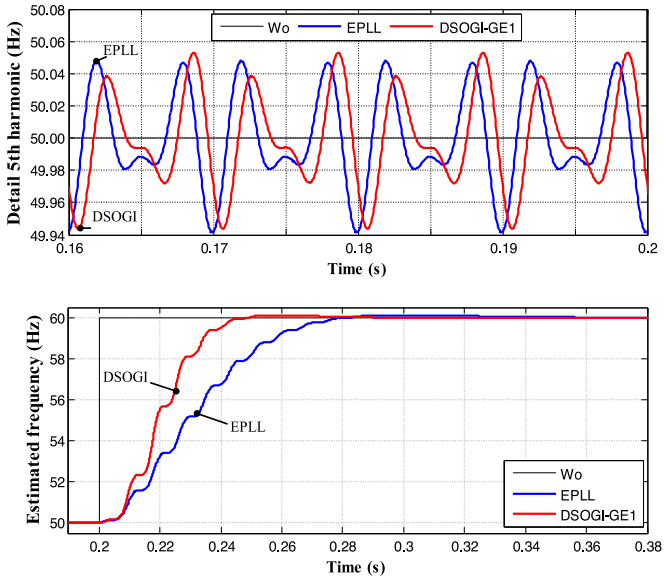

Fig. 16. Up: Equal EPLL and DSOGI-GE_1 peak-to-peak amplitude distortions of the estimated frequency for a 5th harmonic with 10% amplitude. Up: Peak-to-peak frequency amplitude distortion. Down: EPLL and DSOGI-GE_1 frequency transient responses to a grid frequency step perturbation from 50 to 60 Hz.

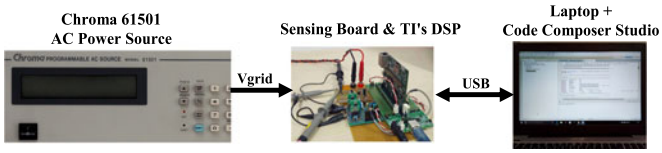

Fig. 17. Experimental setup.

response of the DSOGI-GE_1 regarding the EPLL. This indicates that the DSOGI-GE_1 can likewise be adequate for applications involving highly distorted waveforms where the transient time response is a matter of concern. For example, this could be the case of two paralleled droop controlled single-phase inverters sharing a nonlinear load, where the active and reactive powers P and Q must be calculated from distorted voltages and currents and the speed of the P–Q calculation scheme determines the system stability and the speed response to load transients.

V. Experimental Results

The experimental results were obtained using a Chroma 61501 single-phase programmable ac power source, an analog sensing prototype board wired to a Texas Instruments (TI) Concerto F28M35H52C1 DSP control board, and a personal computer with Code Composer Studio software from TI (see Fig. 17). The prototype included a digital-to-analog-converter (DAC) chip wired with a series serial peripheral interface (SPI) communication protocol to the DSP control board. The DAC allowed displaying up to four DSP internal variables in real-time within a 0–3 V output voltage window. There was a sensing circuit that accommodated the grid voltage to the required 3 V ADC window of the TI's DSP.

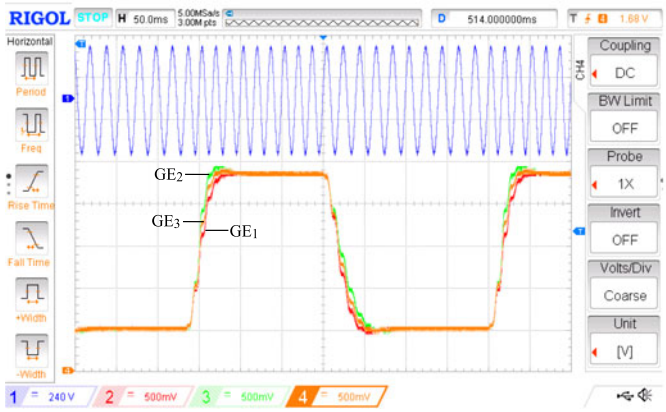

Fig. 18. Experimental results for the DSOGI-GEs estimation of a square wave frequency between 50 and 60 Hz with period 0.37 s. Channel 1: Grid voltage (240 V/div, 50 ms/div). Channels 2–4: Estimated frequencies (500 mV/div or 2.3 Hz/div, 50 ms/div). Channel correspondence: Channel 2 to GE_1, Channel 3 to GE_2, and Channel 4 to GE_3.

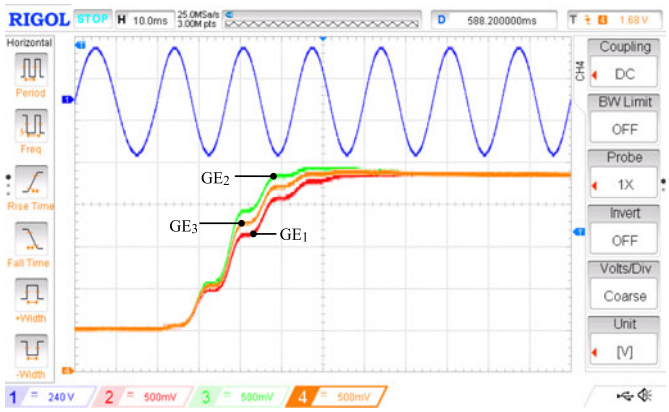

Fig. 19. Step-up transient response detail of Fig. 13. Channel 1: Grid voltage (240 V/div, 10 ms/div). Channels 2–4: Estimated frequencies (500 mV/div or 2.3 Hz/div, 10 ms/div). Channel correspondence: Channel 2 to GE_1, Channel 3 to GE_2, and Channel 4 to GE_3.

The sampling frequency was 20 kHz and the DSOGI-GEs were discretized and implemented using a Backward Euler algorithm [45]. The parameters were set to $\xi = 0.7$ and $\lambda = 49.3(\mathrm{s}^{-1})$ as in the performed simulations. The three proposed DSOGI-GEs (31)–(33) were implemented in the TI's floating point DSP and executed in parallel in order to compare the results. Experimental results were obtained to show the DSOGI-GEs response to a frequency step, harmonic, dc-offset voltage, and voltage sag perturbations. Experiments with subharmonics were not performed due to the high-rejection capability of the DSOGI-GEs structure.

A sinusoidal 220 V (rms) grid voltage with frequency varying according a square wave between 50 and 60 Hz with period 0.37 s was programmed first in the ac source. Fig. 18 shows the grid voltage and the three obtained DSOGI-GEs estimated frequency outputs, meanwhile Figs. 19 and 20 show a detailed capture of the step-up and step-down transients. The displayed frequency signals were centered and amplified in order to fit them as much as possible to the 3 V DAC output window, so the vertical axis 500 mV/div gain corresponded to 2.3 Hz/div

Fig. 20. Step-down transient response detail of Fig. 13. Channel 1: Grid voltage (240 V/div, 10 ms/div). Channels 2–4: Estimated frequencies (500 mV/div or 2.3 Hz/div, 10 ms/div). Channel correspondence: Channel 2 to GE_1, Channel 3 to GE_2, and Channel 4 to GE_3.

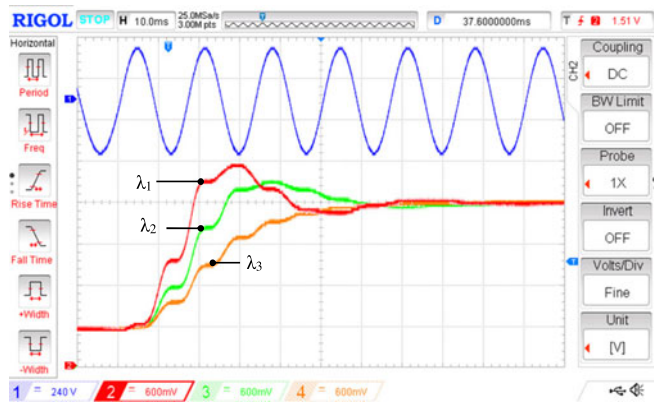

Fig. 21. Experimental results for the DSOGI-GE_1 estimation of a square wave frequency between 50 and 60 Hz with period 0.8 s and for three GE_1 different gains $\lambda_1 = 119.3$, $\lambda_2 = 72.2$, and $\lambda_3 = 42.4$. Channel 1: Grid voltage (240 V/div, 10 ms/div). Channels 2–4: Estimated frequencies (600 mV/div or 3.33 Hz/div, 10 ms/div).

in this case. The responses overshoots were measured using the DSP defined internal variables and were close to the obtained ones in the simulations, which ranged from 1% for GE_1 to 4% for GE_2.

Alternatively, Fig. 21 shows the experimental results for achieving three different transient responses with GE_1, corresponding to the used in the simulations of Fig. 9. The measured overshoots are of 30.8%, 15.4%, and 0% for λ_1, λ_2, and λ_3, respectively, which are close to the obtained in Fig. 9. The scope vertical gain is 3.33 Hz/div.

A third harmonic with 10% amplitude and 0° phase was added to the fundamental 50-Hz grid voltage programmed in the ac source. Fig. 22 depicts the resulting grid voltage and the DSOGI-GEs estimated frequency responses. These signals were accommodated again to the 3 V DAC output window. In this case, the scope vertical gain corresponded to 0.22 Hz/div. The measured peak-to-peak amplitudes of the distortions in the estimated frequencies were 0.30, 0.31, and 0.30 Hz for GE_1, GE_2, and GE_3, respectively.

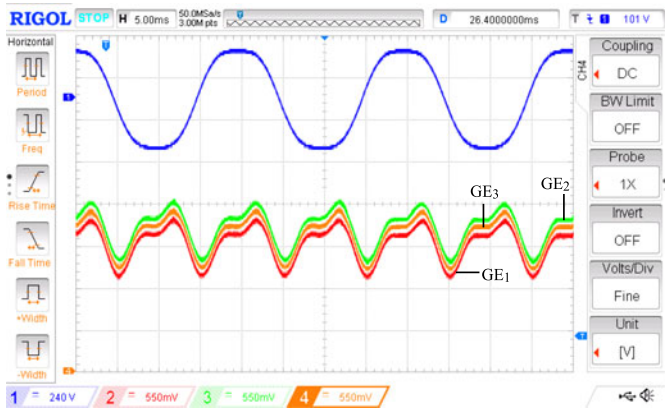

Fig. 22. Experimental response to a grid voltage with a 3rd harmonic of 10% amplitude. Channel 1: Grid voltage (240 V/div, 10 ms/div). Channels 2–4: Estimated frequencies (550 mV/div or 0.22 Hz/div, 5 ms/div). Channel correspondence: Channel 2 to GE_1, Channel 3 to GE_2, and Channel 4 to GE_3.

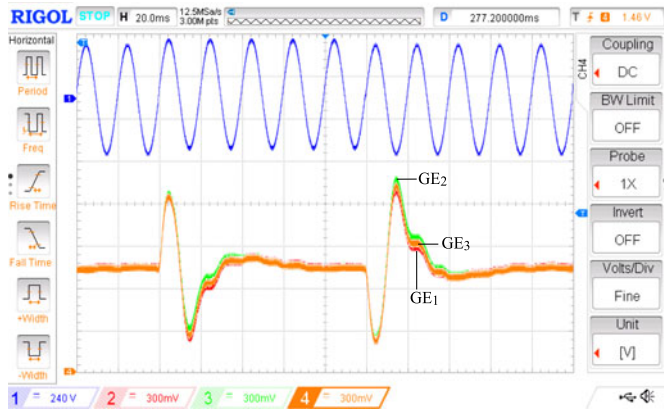

Fig. 23. Experimental response to a dc-offset voltage perturbation of 10% nominal amplitude. Channel 1: Grid voltage (240 V/div, 20 ms/div). Channels 2–4: Estimated frequencies (300 mV/div or 0.16 Hz/div, 20 ms/div). Channel correspondence: Channel 2 to GE_1, Channel 3 to GE_2, and Channel 4 to GE_3.

A repetitive dc-offset voltage perturbation with a 10% amplitude from nominal and width of 0.1 s was programmed in the ac source. Fig. 23 depicts the grid voltage and the DSOGI-GEs estimated frequency response. The DSOGI-GEs signals were accommodated to the 3 V DAC output window, which led to a 0.16 Hz/div for the vertical scope gain. As in the simulation results, the perturbation disappears after 80 ms and the measured peak magnitudes of the estimated frequencies are below 0.3 Hz.

Then, an 80% depth periodic voltage sag perturbation for the grid voltage was programmed in the ac source. Fig. 24 depicts the resulting grid voltage and the DSOGI-GEs estimated frequency responses.

In Fig. 24, the signals were accommodated again to the 3 V DAC output window. In this case, the scope vertical gain corresponded to 2.28 Hz/div. The transients lasted about 80 ms as in the simulations and the measured peak-to-peak amplitudes of the frequency perturbations were 6.31, 6.32, and 6.40 Hz for GE_1, GE_2, and GE_3, respectively (see Table X).

Finally, Fig. 25 shows the grid voltage estimated amplitudes for the same 80% depth voltage sag perturbation. In this case, the correspondence of the scope gain was 59.8 V/div due to

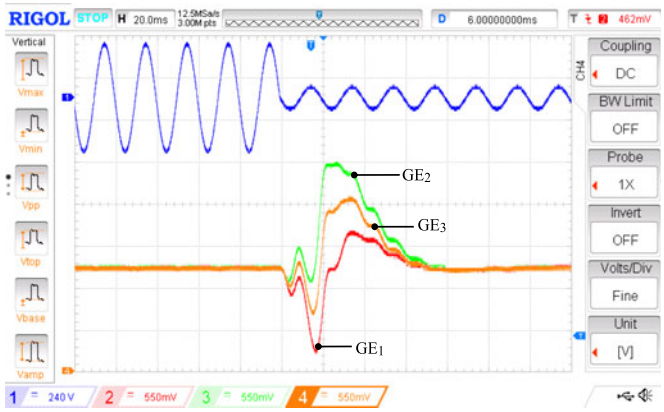

Fig. 24. Experimental results of the DSOGI-GEs estimated frequencies for a periodic 80% depth voltage sag. Channel 1: Grid voltage (240 V/div, 20 ms/div). Channels 2–4: Estimated frequencies (450 mV/div or 2.28 Hz/div, 20 ms/div). Channel correspondence: Channel 2 to GE_1, Channel 3 to GE_2, and Channel 4 to GE_3.

TABLE X
DSOGI-GEs EXPERIMENTALLY MEASURED CHARACTERISTICS OF THE FREQUENCY PERTURBATIONS FOR AN 80% DEPTH VOLTAGE SAG

	GE_1	GE_2	GE_3
DSOGI-GEs upper peak from 50 Hz (Hz)	1.92	3.75	5.67
DSOGI-GEs lower peak from 50 Hz (Hz)	4.39	2.47	0.73
DSOGI-GEs peak-to-peak amplitude (Hz)	6.31	6.22	6.40

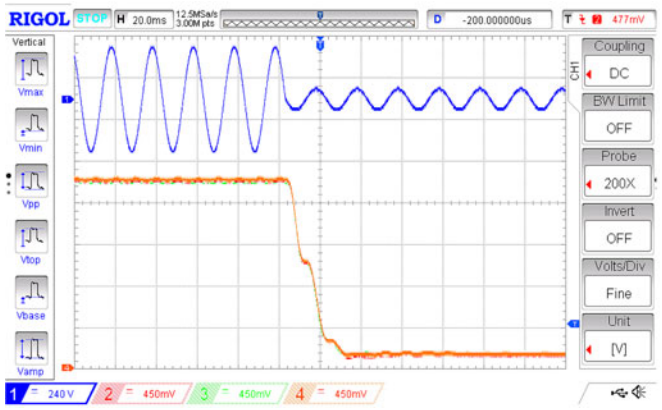

Fig. 25. Experimental results of the DSOGI-GEs estimated voltage amplitudes for a periodic 80% depth voltage sag. Channel 1: Grid voltage (240 V/div, 20 ms/div). Channels 2–4: Estimated grid voltage amplitudes (450 mV/div or 59.8 V/div, 20 ms/div). Channel correspondence: Channel 2 to GE_1, Channel 3 to GE_2, and Channel 4 to GE_3.

the DAC 3 V accommodation. All the obtained responses were close to each other and the perturbation was detected after 28 ms, which is similar to the simulation case.

VI. CONCLUSION

This paper applied the gradient descent method to the SOGI filter in order to find an online estimation for the grid frequency. The method led to three different simple algorithms that can be used to tune the SOGI filter. One of them is identical to the FLL approach reported in literature in the SOGI-FLL, DSOGI-FLL, DSOGI-FLL-WPF, and MSOGI-FLL structures, which point out that the FLL is in fact a gradient descent estimator and not a frequency locked loop. Therefore, as a theoretical result it is concluded that the FLL should be placed under the adaptive control theory paradigm.

The SOGI-GEs behavior has been analyzed in front of grid distortions, showing problems specially in the case of subharmonics and dc-offset voltage. A DSOGI approach has been proposed to remove these problems. The analysis of the DSOGI-GEs has shown that it provides a better harmonic rejection capability and an improved response to deep voltage sags than the SOGI-FLL, but at the cost of an additional acceptable delay in the transient response to step frequency changes. As a strong point, it should be remarked that the DSOGI-GEs have a high rejection capability for harmonics, especially for those of higher orders, and a good tradeoff relationship between harmonic rejection and transient response speed. Then, the DSOGI-GEs structures are adequate for applications subjected to high harmonic distortion in which the rejection to harmonics is an important issue. It also shows to be adequate for applications requiring the extraction of a fundamental component from highly distorted waveforms, such as the case of pulsating currents drawn by *RC*-rectifier type nonlinear loads.

Experimental results have been provided using a TI's floating point DSP, a sensing board, an analog DAC, and a programmable ac power source. The experimental results agree with the simulated ones, which validates the gradient descent proposal.

APPENDIX

Considering GI, the transfer function from v_a to v_e is

$$\frac{v_a(s)}{v_e(s)} = \frac{s^2}{s^2+\omega^2} \tag{35}$$

and introducing the time expression of (35) in (16), it gives

$$\frac{d\omega}{dt} = \frac{\gamma}{\omega}(v_a + \omega^2 \int \left(\int v_a d\tau\right) \cdot d\tau) \cdot v_a. \tag{36}$$

For an input as (20), at steady state it holds $\int (\int v_a d\tau) \cdot d\tau = -\frac{v_a}{\omega_o^2}$ and $v_a = \mathrm{A}G_a(j\omega_o,\omega)\cos(\omega_0 t + \varphi + \varphi_d)$, where $G_a(j\omega_o,\omega)$ is the gain of (3) and φ_d is the phase of (1). Then, the update law can be approximated as

$$\begin{aligned}\frac{d\omega}{dt} &= -\frac{\gamma}{\omega\omega_o^2}(\omega^2-\omega_o^2)v_a^2 \\ &= -\frac{\gamma}{\omega\omega_o^2}(\omega^2-\omega_o^2)A^2G_a^2(j\omega_o,\omega)\cos^2(\omega_o t+\varphi+\varphi_d).\end{aligned} \tag{37}$$

Thus, calculating the averaged value of (37) it is obtained

$$\frac{d\omega_{\mathrm{av}}}{dt} = -\gamma\frac{2\xi^2A^2\omega_o^2(\omega_{\mathrm{av}}^2-\omega_o^2)}{\omega_{\mathrm{av}}\left((\omega_{\mathrm{av}}^2-\omega_o^2)^2+(2\xi\omega_{\mathrm{av}}\omega_o)^2\right)} \tag{38}$$

whose first-order linearization around its isolated equilibrium point $\omega_{\mathrm{av}} = \omega_{\mathrm{o}}$ results in the same asymptotically stable dynamics (27).

REFERENCES

[1] C. L. Chen, Y. Wang, J. S. Lai, Y. S. Lee, and D. Martin, "Design of parallel inverters for smooth mode transfer microgrid applications," *IEEE Trans. Power Electron.*, vol. 25, no. 1, pp. 6–15, Jan. 2010.

[2] D. M. Vilathgamuwa, P. C. Loh, and Y. Li, "Protection of microgrids during utility voltage sags," *IEEE Trans. Ind. Electron.*, vol. 53, no. 5, pp. 1427–1436, Oct. 2006.

[3] G. Yalcinkaya, M. H. J. Bollen, and P. A. Crossley, "Characterization of voltage sags in industrial distribution systems," *IEEE Trans. Ind. Appl.*, vol. 34, no. 5, pp. 682–688, Jul. 1998.

[4] M. H. Bollen, "Algorithms for characterizing measured three-phase unbalanced voltage dips," *IEEE Trans. Power Del.*, vol. 18, no. 3, pp. 937–944, Jul. 2003.

[5] H. Song and K. Nam, "Dual current control scheme for PWM converter under unbalanced input voltage conditions," *IEEE Trans. Ind. Electron.*, vol. 46, no. 5, pp. 953–959, Oct. 1999.

[6] *IEEE Standard for Interconnecting Distributed Resources With Electric Power Sys*tems, IEEE Standard 1547, 2003.

[7] P. Roncero-Sanchez, X. del Toro Garcia, A. P. Torres, and V. Feliu, "Robust frequency-estimation method for distorted and imbalanced three-phase systems using discrete filters," *IEEE Trans. Power Electron.*, vol. 26, no. 4, pp. 1089–1101, Apr. 2011.

[8] S. K. Chung, "A phase tracking system for three phase utility interface inverters," *IEEE Trans. Power Electron.*, vol. 15, no. 3, pp. 431–438, May 2000.

[9] J. Svensson, "Synchronization methods for grid-connected voltage source converters," *Proc. Inst. Elect. Eng.—Gener. Transmiss. Distrib.*, vol. 148, no. 3, pp. 229–235, May 2001.

[10] M. Karimi-Ghartemani and M. R. Iravani, "A nonlinear adaptive filter for online signal analysis in power systems applications," *IEEE Trans. Power Del.*, vol. 17, no. 2, pp. 617–622, Apr. 2002.

[11] M. Karimi-Ghartemani and M. R. Iravani, "A method for synchronization of power electronic converters in polluted and variable-frequency environments," *IEEE Trans. Power Syst.*, vol. 19, no. 3, pp. 1263–1270, Aug. 2004.

[12] M. Karimi-Ghartemani, H. Karimi, and M. R. Iravani, "A magnitude phase-locked loop system based on estimation of frequency and in-phase quadrature-phase amplitudes," *IEEE Trans. Ind. Electron.*, vol. 51, no. 2, pp. 511–517, Apr. 2004.

[13] H. Karimi, M. Karimi-Ghartemani, and M. R. Iravani, "Estimation of frequency and its rate of change for applications in power systems," *IEEE Trans. Power Del.*, vol. 19, no. 2, pp. 472–480, Apr. 2004.

[14] D. Yazdani, A. Bakhshai, and P. K. Jain, "A three-phase adaptive notch filter-based approach to harmonic/reactive current extraction and harmonic decomposition," *IEEE Trans. Power Electron.*, vol. 25, no. 4, pp. 914–923, Apr. 2010.

[15] F. D. Freijedo, J. Doval-Gandoy, O. López, and E. Acha, "Tuning of phase-locked loops for power converters under distorted utility conditions," *IEEE Trans. Ind. Appl.*, vol. 45, no. 6, pp. 2039–2047, Nov./Dec. 2009.

[16] N. Hoffmann, R. Lohde, M. Fischer, F. W. Fuchs, L. Asiminoaei, and P. B. Thogersen, "A review on fundamental grid-voltage detection methods under highly distorted conditions in distributed power-generation networks," in *Proc. Energy Convers. Congr. Expo.*, 2011, pp. 3045–3052.

[17] E. Robles, J. Pou, S. Ceballos, J. Zaragoza, J. L. Martin, and P. Ibañez, "Frequency-adaptive stationary-reference-frame grid voltage sequence detector for distributed generation systems," *IEEE Trans. Ind. Electron.*, vol. 58, no. 9, pp. 4275–4287, Sep. 2011.

[18] M. A. Perez, J. R. Espinoza, L. A. Moran, M. A. Torres, and E. A. Araya, "A robust phase-locked loop algorithm to synchronize static-power converters with polluted AC systems," *IEEE Trans. Power Electron.*, vol. 55, no. 5, pp. 2185–2192, May 2008.

[19] F. Gonzalez-Espin, E. Figueres, and G. Garcera, "An adaptive synchronous-reference-frame phase-locked loop for power quality improvement in a polluted utility grid," *IEEE Trans. Ind. Electron.*, vol. 59, no. 6, pp. 2718–2731, Jun. 2012.

[20] Z. Qi, S. Xiang-Dong, Z. Yan-Ru, M. Matsui, and R. Bi-Ying, "Analysis and design of a digital phase-locked loop for single-phase grid-connected power conversion systems," *IEEE Trans. Ind. Electron.*, vol. 58, no. 8, pp. 3581–3592, Aug. 2011.

[21] T. Thacker, D. Boroyevich, R. Burgos, and F. Wang, "Phase-locked loop noise reduction via phase detector implementation for single-phase systems," *IEEE Trans. Ind. Electron.*, vol. 58, no. 6, pp. 2482–2490, Jun. 2011.

[22] M. Ciobotaru, R. Teodorescu, and F. Blaabjerg, "A new single-phase PLL structure based on second order generalized integrator," in *Proc. Power Electron. Spec. Conf.*, Jun. 2006, pp. 1–7.

[23] U. Nuβ, "Blindleistungskompensation mit selbsgeführtem stromrichter und kapazitivem energiespeicher," Dissertation am elektrotechnischen institut der Universität Karlsruhe, Karlsruhe, Germany, 1989.

[24] B. Burger and A. Engler, "Fast signal conditioning in single phase systems," in *Proc. Eur. Conf. Power Electron. Appl.*, 2001, pp. 1–10.

[25] X. Yuan, W. Merk, H. Stemmler, and J. Allmeling, "Stationary-frame generalized integrators for current control of active power filters with zero steady-state error for current harmonics of concern under unbalanced and distorted operating conditions," *IEEE Trans. Ind. Appl.*, vol. 38, no. 2, pp. 523–532, Mar./Apr. 2002.

[26] S. Golestan, J. M. Guerrero, and J. C. Vasquez, "Single-phase PLLs: A review of recent advances," *IEEE Trans. Power Electron.*, vol. 32, no. 12, pp. 9013–9030, Dec. 2017.

[27] P. Rodriguez, A. Luna, M. Ciobotaru, R. Teodorescu, and F. Blaabjerg, "Advanced grid synchronization system for power converters under unbalanced and distorted operating conditions," in *Proc. Annu. Conf. IEEE Ind. Electron.*, 2006, pp. 5173–5178.

[28] P. Rodriguez, A. Luna, I. Candela, R. Teodorescu, and F. Blaabjerg, "Grid synchronization of power converters using multiple second order generalized integrators," in *Proc. Annu. Conf. IEEE Ind. Electron.*, 2008, pp. 755–760.

[29] P. Rodriguez, A. Luna, I. Candela, R. Mujal, R. Teodorescu, and F. Blaabjerg, "Multiresonant frequency-locked loop for grid synchronization of power converters under distorted grid conditions," *IEEE Trans. Ind. Electron.*, vol. 58, no. 1, pp. 127–138, Jan. 2011.

[30] P. Rodriguez, A. Luna, I. Etxebarria, R. Teodorescu, and F. Blaabjerg, "A stationary reference frame grid synchronization system for three-phase grid-connected power converters under adverse grid conditions," *IEEE Trans. Ind. Electron.*, vol. 27, no. 1, pp. 99–112, Jan. 2012.

[31] M. Karimi Ghartemani, S. A. Khajehoddin, P. K. Jain, and A. Bakhshai, "Problems of startup and phase jumps in PLL systems," *IEEE Trans. Power Electron.*, vol. 27, no. 4, pp. 1830–1838, Apr. 2012.

[32] M. Karimi Ghartemani, S. A. Khajehoddin, P. K. Jain, A. Bakhshai, and M. Mojiri, "Addressing DC component in PLL and notch filter algorithms filter algorithms," *IEEE Trans. Power Electron.*, vol. 27, no. 1, pp. 78–86, Jan. 2012.

[33] T. Ngo, Q. Nguyen, and S. Santoso, "Improving performance of single-phase SOGI-FLL under DC-Offset voltage condition," in *Proc. Annu. Conf. IEEE Ind. Electron. Soc.*, 2015, pp. 1537–1541.

[34] J. S. Park, T. H. Nguyen, and D. C. Lee, "Advanced SOGI-FLL scheme based on fuzzy logic for single-phase grid-connected converters," *J. Power Electron.*, vol. 14, no. 3, pp. 598–607, May 2014.

[35] S. Golestan, E. Ebrahimzadeh, J. M. Guerrero, and J. C. Vasquez, "An adaptive resonant regulator for single-phase grid-tied VSCs," *IEEE Trans. Power Electron.*, vol. PP, no. 99, Aug. 9, 2017, doi: 10.1109/TPEL.2017.2736945.

[36] J. Matas, M. Castilla, J. Miret, L. G. de Vicuna, and R. Guzman, "An adaptive prefiltering method to improve the speed/accuracy tradeoff of voltage sequence detection methods under adverse grid conditions," *IEEE Trans. Ind. Electron.*, vol. 61, no. 5, pp. 2139–2151, May 2014.

[37] J. Matas, M. Castilla, L. G. Vicuna, J. Miret, E. Alarcón-Gallo, and A. Camacho, "Fast grid synchronization technique based on a multiple cascaded general integrator scheme for distributed generation inverters," in *Proc. Int. Symp. Ind. Electron.*, Jun. 2012, pp. 1003–1010.

[38] M. Rashed, C. Klumpner, and G. Asher, "Dynamic phasor analysis and design of phase-locked loops for single phase grid connected converters," *COMPEL Int. J. Comput. Math. Elect. Electron. Eng.*, vol. 34, no. 4, pp. 1122–1143, Jul. 2015.

[39] S. Reza, M. Ciobotaru, and V. G. Agelidis, "Accurate estimation of single-phase grid voltage fundamental amplitude and frequency by using a frequency adaptive linear Kalman filter," *IEEE J. Emerg. Sel. Topics Power Electron.*, vol. 4, no. 4, pp. 1226–1235, Dec. 2016.

[40] S. Sastry and M. Bodson, *Adaptive Control: Stability, Convergence, and Robustness*. New York, NY, USA: Dover, 2011.

[41] P. Ioannou and J. Sung, *Robust Adaptive Control*. New York, NY, USA: Dover, 2012.

[42] J. A. Sanders, F. Verhulst, and J. Murdock, *Averaging Methods in Nonlinear Dynamical Systems*, 2nd ed. New York, NY, USA: Springer, 2007.

[43] F. Verhulst, *Nonlinear Differential Equations and Dynamical Systems*, 2nd ed. New York, NY, USA: Springer, 2000.

[44] M. Karimi-Ghartemani, *Enhanced Phase-Locked Loop Structures for Power and Energy Applications*. Piscataway, NJ, USA: IEEE Press, 2014.

[45] F. J. Rodriguez, E. Bueno, M. Aredes, L. G. B. Rolim, F. A. S. Neves, and M. C. Cavalcanti, "Discrete-time implementation of second order generalized integrators for grid converters," in *Proc. Annu. Conf. IEEE Ind. Electron.*, 2008, pp. 176–181.

José Matas received the B.S., M.S., and Ph.D. degrees in telecommunications engineering from the Technical University of Catalonia, Barcelona, Spain, in 1988, 1996, and 2003, respectively.

From 1988 to 1990, he was an Engineer in a consumer electronics company. Since 1990, he has been an Associate Professor in the Department of Electronic Engineering, Technical University of Catalonia, where he enrolled to the Department of Electrical Engineering in 2017. His research interests include power electronics, nonlinear control, power quality, renewable energy systems, and microgrids.

Helena Martín received the B.Sc. degree in electronic engineering in 1994, the M.Sc. degree in electrical engineering in 1997, and the Ph.D. degree in industrial engineering in 2007 from Technical University of Catalonia.

She is currently an Associate Professor with the Department of Electric Engineering, Technical University of Catalonia, Barcelona, Spain. Her research interests include microgrids control, optimal management and energy policy for microgids with renewable energy generation.

Jordi de la Hoz received the B.Sc. degree in electrical engineering, the M.Sc. degree in industrial electronics and automatic control, and the Ph.D. degree in industrial engineering from the Technical University of Catalonia (UPC), Barcelona, Spain, in 1998, 2002, and 2009, respectively.

Since 2001, he has been with the Electrical Engineering Department, UPC. His current research focuses on the analysis of the impact that the regulatory frameworks have on the development, design, and management of renewable energy systems (including microgrids).

Abdullah Abusorrah (M'08–SM'14) received the B.S. and M.S. degrees from King Abdulaziz University, Jeddah, Saudi Arabia, in 1994 and 2002, respectively, and the Ph.D. degree from the University of Nottingham, Nottingham, U.K., in 2007, all in electrical engineering.

He is currently an Associate Professor in the Department of Electrical and Computer Engineering and the Head of Renewable Energy Research Group, King Abdulaziz University. His research interests include power quality, smart grid, and system analyses.

Yusuf A. Al-Turki (M'90–SM'17) received the Ph.D. degree in power systems from the University of Manchester, Manchester, U.K., in 1985.

Since 1999, he has been a Professor with the Department of Electrical and Computer Engineering, King Abdulaziz University, Jeddah, Saudi Arabia, where he is currently the Vice president of King Abdulaziz University for Postgraduate studies and scientific research. His research interests include system modeling, power system dynamics, renewable energy, and microgrids.

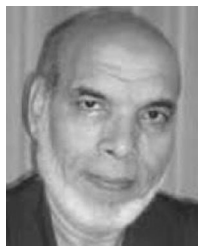

Mohammed Al-Hindawi received the Ph.D. degree in power electronics from Cairo University, Giza, Egypt, in 1981.

He is currently an Associate Professor in the Department of Electrical and Computer Engineering, King Abdulaziz University, Jeddah, Saudi Arabia. His research interests include power electronics converters and microgrids.